

1 Heliosheath fluctuations near the
2 perpendicular termination shock:
3 two-dimensional hybrid simulations

Kaijun Liu, S. Peter Gary, and Dan Winske

4 Los Alamos National Laboratory, Los Alamos, New Mexico

Kaijun Liu, S. Peter Gary, and Dan Winske, Los Alamos National Laboratory, Los Alamos,
NM 87545. (e-mail: kaijun@lanl.gov, pgary@lanl.gov, winske@lanl.gov)

Abstract. The two-dimensional Los Alamos hybrid simulation code is used to study the excitation of fluctuations and the associated ion dynamics at the high Alfvén-Mach heliospheric termination shock and in the near-shock heliosheath. This simulation represents the electrons as a zero-mass fluid, addresses only a perpendicular shock, and considers the upstream ions to consist of a cool solar wind component and a more energetic pickup component. The shock yields two strongly heated downstream components: the more dense thermals and the more tenuous suprathermals, each with strong $T_{\perp} > T_{\parallel}$ anisotropies. In the downstream, relatively homogeneous sheath plasma, linear dispersion theory predicts that each component anisotropy drives both the Alfvén-cyclotron instability and the proton mirror instability. The simulation demonstrates that Alfvén-cyclotron modes dominate mirror-like modes in the downstream, in contrast to earlier two-dimensional hybrid simulations of high-Mach quasi-perpendicular shocks without pickup ions, in which the Alfvén-cyclotron and mirror modes were excited to comparable intensities. A hypothesis is presented that the presence of pickup ions implies a relatively low magnetosonic Mach number at termination shocks, thereby favoring the excitation of the Alfvén-cyclotron instability. The primary consequence of wave-particle interactions from this instability is pitch-angle scattering, so the energetic part of the ion perpendicular velocity distribution in the heliosheath is depleted by comparison with the distribution computed from a comparable one-dimensional hybrid simulation.

1. Introduction

As the solar wind flows away from the Sun, interstellar neutral particles, primarily hydrogen, become ionized, are picked up and become part of the flow. So in the outer heliosphere the flowing plasma primarily consists of a more dense, relatively cool ($T \sim$ eV) solar wind ion component, and a more tenuous, more energetic (\sim keV) pickup ion component. The decreasing energy density of this outward flowing plasma leads to a transition from supersonic to subsonic flow; this is the termination shock where the flowing plasma is compressed and heated.

The Voyager 1 spacecraft crossed the termination shock in 2004 [Stone *et al.*, 2005; Burlaga *et al.*, 2005] and Voyager 2 made a number of crossings of the shock in late 2007 [Stone *et al.*, 2008; Burlaga *et al.*, 2008]. The Voyager 2 crossings were notable in that low-energy (< 10 eV) plasma measurements, as well as magnetic field measurements, were available, so that heating of the thermal ion component was measured. The magnetic field profiles, especially those of the TS-2 crossing of Voyager 2, showed a well-defined shock structure, including an extended rise of the magnetic field (“foot”) upstream, a sharp rise of the magnetic field (“ramp”) at the shock itself, and a peak of the magnetic field at the end of the ramp (“overshoot”) that is larger than the average downstream value. Such features are also characteristic of quasi-perpendicular bow shock crossings for upstream Alfvén Mach numbers larger than a critical value (a “supercritical shock”) [e.g. Greenstadt *et al.*, 1980; Bale, 2005].

However, neither Voyager spacecraft directly measured the properties of the pickup ions, and so we have no *in situ* observations of the response of these ions to the termination

shock and its environs. Ion kinetic simulations of the termination shock reproduce the qualitative observed features of the shock crossing [Liewer *et al.*, 1993; Lee *et al.*, 2005; Wu *et al.*, 2009], indicating how the pickup ions modify the basic spatial scales of the shock and how plasma flow energy dissipated at the shock is partitioned between the pickup and solar wind ions. But we do not have, and are not likely to soon obtain, detailed measurements of species velocity distributions at and near this shock.

Beyond the termination shock lies the heliosheath, where the plasma is further processed by wave-particle scattering and by charge-exchange with the interstellar neutrals. Quasi-perpendicular shocks drive ion heating preferentially perpendicular to the background magnetic field; this excites instabilities which, via wave-particle scattering, reduces the ion anisotropy. Charge-exchange between the heated ions and cold interstellar neutrals leads to an enhanced flux of energetic neutral particles, predominantly hydrogen, which propagate away from this region unaffected by the electromagnetic fields of the interplanetary and interstellar medium.

The Interstellar Boundary Explorer, or IBEX [McComas *et al.* 2004], is an Earth-orbiting satellite with the primary objective of studying the global interaction between the solar wind and the interstellar medium. IBEX carries two highly sensitive Energetic Neutral Atom (ENA) imaging instruments which measure neutral particles in two energy bands, 10 eV to 2 keV and 300 eV to 6 keV. In look directions away from the vicinity of the Earth, the primary source of such neutrals is the inner heliosheath; by imaging these neutral particles, IBEX is providing new information about how our heliosphere interacts with the interstellar medium which surrounds it [McComas *et al.*, 2009; Funsten *et al.*, 2009]. Heating at the termination shock and subsequent scattering in the heliosheath

determine the velocity distributions of the protons which in turn determine the fluxes of the ENAs measured by IBEX.

Downstream of the quasi-perpendicular terrestrial bow shock, both observations [*Anderson et al.*, 1994; *Farrugia et al.*, 2005] and simulations [*Thomas and Brecht*, 1986, 1987; *Winske and Quest*, 1988; *McKean et al.*, 1995, 1996] have demonstrated strong ion anisotropies of the type $T_{\perp}/T_{\parallel} > 1$, leading to enhanced field fluctuations from both the Alfvén-cyclotron and proton mirror instabilities. Observations of the magnetic field in the heliosheath have been made from both Voyager 1 and 2 [*Burlaga et al.*, 2005; 2008], showing large amplitude compressive fluctuations called magnetic holes [*Burlaga et al.*, 2007]. But to date there are no reported measurements of thermal ion anisotropies or corresponding instability-driven enhanced fluctuations in the heliosheath. Alfvén-cyclotron and mirror-like fluctuations scatter ions differently, so it is important to determine their relative amplitudes in the heliosheath if we are to predict the properties of ions heated by the termination shock and the consequent ENA fluxes which emanate from this region.

Just as the upstream ions consist of two distinct components, the more dense, cooler solar wind (denoted by subscript *sw*) and the more tenuous, hotter pickup ions (denoted by subscript *pu*), termination shock simulations show that the heated downstream ions also consist of two distinct components [*Wu et al.*, 2010]. In our treatment of linear theory as applied to downstream instabilities described in the Appendix, we follow *Wu et al.* [2010] and use the adjective “thermal” (subscript *t*) to denote the more dense, relatively cool ions and “suprathernal” (subscript *s*) to denote the more tenuous, hotter ions. However, in our simulations we can label and then follow each upstream ion and distinguish solar wind from pickup components in the downstream. Relatively few solar wind ions are

accelerated by the shock up to suprathermal energies, so in Section 4 and Section 5 we continue to use the terms “solar wind” and “pickup” to refer to the respectively cooler and hotter downstream ion components, with the understanding that these are approximately equivalent to the corresponding labels of thermal and suprathermal.

This manuscript describes two-dimensional hybrid simulations of the perpendicular termination shock with emphasis on the excitation of enhanced fluctuations at and downstream of the shock. Our particular interest here is how these fluctuations interact with the few KeV suprathermal ions which are a primary source of ENA fluxes measured by IBEX instrumentation. Section 2 summarizes relevant results from earlier simulations. Section 3 reviews properties of the Los Alamos hybrid simulation code, Section 4 describes general plasma results from the simulations, and Section 5 discusses the fluctuating fields resulting from the computations. Section 6 presents a summary and a conclusion, while Appendix A presents results of linear theory for instabilities downstream of the simulated shocks.

We denote the ion plasma frequency as $\omega_i \equiv \sqrt{4\pi n_o e^2 / m_i}$, the ion cyclotron frequency as $\Omega_i \equiv e_i B_o / m_i c$, the ion inertial length $\lambda_i \equiv c / \omega_i$, and the β of the j th ion component as $\beta_{\parallel j} \equiv 8\pi n_j k_B T_{\parallel j} / B_o^2$. The Alfvén speed is $v_A = B_o / \sqrt{4\pi n_o m_i}$. Here n_o is the total upstream plasma density and \mathbf{B}_o denotes the upstream uniform background magnetic field. The Cartesian coordinate systems of our two-dimensional simulations and of linear dispersion theory are the same; there are spatial variations in both the direction parallel to \mathbf{B}_o (denoted by \parallel) and one direction perpendicular to the background field (denoted by \perp), but no spatial variations in the other perpendicular direction (denoted by $\perp\perp$).

116 Here θ denotes the angle between \mathbf{k} and \mathbf{B}_o : $\hat{\mathbf{k}} \cdot \hat{\mathbf{B}}_o = \cos(\theta)$. In the simulation, $\hat{\mathbf{x}}$ is the
 117 \perp direction, $\hat{\mathbf{y}}$ is the \parallel direction, and $\hat{\mathbf{z}}$ is the $\perp\perp$ direction.

2. Previous Simulations

118 The most powerful and most complete tools for understanding the plasma physics of
 119 collisionless shocks are kinetic simulations. There are two distinct categories of such
 120 computations: particle-in-cell (PIC) and hybrid simulations.

121 PIC simulations provide a self-consistent description of the evolution of plasma ions and
 122 electrons as well as the associated electric and magnetic fields. Although one-dimensional
 123 PIC simulations have been applied to the termination shock [*Lee et al.* 2005; *Chapman et*
 124 *al.*, 2005; *Matsukiyo et al.*, 2007], such computations require that the electron dynamics be
 125 followed in detail. This restricts such calculations to relatively short times and, typically,
 126 to one spatial dimension.

127 Hybrid simulations treat ion species as superparticles, but represent electrons as a fluid
 128 while providing a self-consistent treatment of the electric and magnetic fields. Hybrid
 129 codes can run to much longer times and/or in more spatial dimensions than PIC codes,
 130 and thus are well suited for studying ion responses to space plasma disturbances such
 131 as the termination shock. The trade-offs are that hybrid codes cannot describe kinetic
 132 electron physics and represent only fluctuations with frequencies near or below the proton
 133 cyclotron frequency and with wavelengths near or longer than the ion inertial length. But
 134 this is precisely the regime of strong interactions between the waves and the ions, so our
 135 hybrid code is an appropriate tool for studies of ion dynamics in collisionless plasmas.

136 *Liewer et al.* [1993] used a one-dimensional hybrid code to show that for high Mach
 137 number quasi-perpendicular termination shocks, the primary mechanism for pickup ion

energy gain is due to those particles which backstream from downstream to upstream where they gain energy before passing back downstream through the shock. As the shock normal angle becomes less than about 60° , oblique and quasi-parallel shocks develop. For such shocks pickup ion heating becomes more involved; reflected ions propagate back upstream, exciting magnetosonic waves which further scatter and energize the ions [*Liewer et al.* 1993, 1995; *Kucharek and Scholer*, 1995; *Scholer et al.* 2002].

Recently *Wu et al.* [2009; 2010] used the one-dimensional Los Alamos hybrid code to simulate the perpendicular termination shock. *Wu et al.* [2009] developed a modified Rankine-Hugoniot model that included pickup ions to interpret the hybrid simulations. *Wu et al.* [2010] showed that specular reflection of ions [*Zank et al.*, 1996] by the electric field normal to such a shock is not necessary for an initial energy gain of pickup ions; rather, the large gyroradius of these ions enables some of them to return upstream where they gain substantial energy from the motional electric field as they gyrate in the "foot" [*Lee et al.*, 2005; *Chapman et al.*, 2005; *Matsukiyo et al.*, 2007]. Further, *Wu et al.* [2010] demonstrated that faster solar wind flows lead to increased fluxes of ions in the tails of their velocity distributions, consistent with energetic neutral atom observations from IBEX [*Funsten et al.*, 2009].

Almost all kinetic termination shock simulations published to date have considered spatial variations only in one dimension. Such simulations can produce genuine shocks that satisfy the Rankine-Hugoniot relations (e.g., *Wu et al.*, 2009). However, one-dimensional simulations have the fundamental limitation that downstream heating occurs only in the two directions perpendicular to the background magnetic field. Two-dimensional simulations of the quasi-perpendicular bow shock without pickup ions have demonstrated

downstream ion perpendicular temperature anisotropies and associated Alfvén-cyclotron and mirror-like enhanced fluctuations [*Thomas and Brecht*, 1986, 1987; *Winske and Quest*, 1988; *McKean et al.*, 1995, 1996] that scatter the ions and provide heating in all three dimensions. Fully three-dimensional simulations of the perpendicular bow shock (*Thomas*, 1989) show very similar shock structure compared to two-dimensional runs, with slight modifications due to the further relaxing of constraints on the allowable modes. And recent two-dimensional and three-dimensional simulations of the competition between Alfvén-cyclotron and proton mirror instabilities in a uniform plasma modeling the region downstream of the bow shock show differences at late times, as large nonlinear three-dimensional structures can develop from mirror-mode fluctuations [*Shoji et al.*, 2009].

In contrast to the many one-dimensional kinetic simulations, *Giacalone and Decker* [2010] used two-dimensional hybrid simulations of the termination shock with an imposed spectrum of upstream turbulence to address ion acceleration to MeV energies due to the combination of these imposed fluctuations and those which develop self-consistently. In contrast, the two-dimensional simulations of the termination shock described here do not admit an initial spectrum of enhanced fluctuations, but rather investigate in detail the field fluctuations which arise self-consistently at the shock or by Alfvén-cyclotron and proton mirror instability growth downstream.

The Alfvén-cyclotron instability has maximum growth rate at $\mathbf{k} \times \mathbf{B}_o = 0$ and under that condition, it yields only fluctuating magnetic field components in the plane perpendicular to \mathbf{B}_o . Thus enhanced fluctuations from this instability have $k_\perp \simeq 0$ and $\delta B_\parallel \simeq 0$. The proton mirror instability has maximum growth rate at propagation oblique to \mathbf{B}_o , so that $k_\perp \neq 0$ and $k_\parallel \neq 0$, but linear theory demonstrates that the fluctuating magnetic

field components associated with this growing mode lie predominantly in the \parallel - \perp plane;
 thus for mirror-like fluctuations $\delta B_{\perp\perp} \simeq 0$.

The primary wave-particle interaction from enhanced fluctuations from the Alfvén-cyclotron instability is through the ion cyclotron resonance. This implies that the principal consequence of this interaction is pitch-angle scattering of ions near or above the ion thermal speed. In contrast, enhanced fluctuations from the proton mirror instability interact mostly through the Landau resonance on subthermal ions. So, Alfvén-cyclotron wave scattering acts largely on the pickup(upstream)/suprathermal(downstream) ions, whereas mirror mode scattering has its greatest effect on the solar wind(upstream)/thermal(downstream) ion components. To understand the different consequences of these two instabilities we need physical insight into the downstream competition between the two. A prime purpose of the research described here is to provide such insight.

The competition between Alfvén-cyclotron and mirror-like fluctuations downstream of quasi-perpendicular shocks is sometimes expressed in terms of growth rates computed from linear theory [Gary, 1992] and simulations of the instabilities in homogeneous plasmas [McKean *et al.*, 1992; 1994; Shoji *et al.*, 2010]. In this scenario, ion anisotropies driven at the shock are the source of linear instability growth as the plasma flows downstream into the relatively homogeneous sheath, as in the low Alfvén-Mach bow shock simulations of McKean *et al.* [1996]. However, the high Alfvén-Mach bow shock simulations of McKean *et al.* [1995] provided a different picture, in which nonlinear processes immediately at the inhomogeneous shock drive large-amplitude fluctuations which decay as the plasma is convected downstream, where linear theory may be used to identify the modes. The

McKean et al. [1995] simulations of the quasi-perpendicular shock, which do not include pickup ions, show that the Alfvén-cyclotron and proton mirror modes are present at comparable intensities downstream.

3. Los Alamos hybrid simulation code

The two-dimensional Los Alamos hybrid code [*Winske and Omid, 1993; 1996; Winske et al., 2003*] self-consistently computes the evolution of plasma ions, fluid electrons, and the associated fluctuating electric and magnetic fields. This is a robust, well-documented simulation code that has been extensively used to study both fast and slow shocks in space plasmas and other environments [*Winske and Quest, 1988; Yin et al., 2005; Winske and Gary, 2007*]. In this code plasma ions are represented as superparticles, while electrons are treated as a massless, adiabatic fluid with $\gamma = 5/3$. The model allows spatial variations in both the direction of shock propagation perpendicular to \mathbf{B}_o (the x direction) and in the direction parallel to \mathbf{B}_o (the y direction). The x - and y - dimensions of the computational box are $L_x = 400\lambda_i$ and $L_y = 256\lambda_i$, the number of cells in the x - and y dimensions are $N_x = 800$ and $N_y = 256$, and the computational time step $\Omega_i\Delta t = 0.02$.

The simulation is run in the downstream, or heliosheath, plasma frame, so that the incident ions are injected from the left wall with an average right-directed velocity; as these ions approach the right-hand wall, the shock is formed and propagates back to the left. As in *Wu et al.* [2009; 2010], our simulation is of a strictly perpendicular shock; our initial conditions are that the upstream solar wind flow speed v_{sw} corresponds to an Alfvén Mach number $M_A = v_{sw}/v_A = 8$, an upstream solar wind $\beta_{sw} = 0.04$, and an upstream pickup ion relative density of $n_{pu}/n_o = 0.20$. The upstream pickup ion velocity distribution is assumed to be the isotropic (in the solar wind frame) Vasyliunas-

Siscoe distribution [*Vasyliunas and Siscoe*, 1976] modified as in *Wu et al.* [2010] so that

$$f_{pu}(v) \sim 1/v^{3/2}; \text{ here } \beta_{pu} = 8.53.$$

4. Simulation: General results

This section describes some general results from the simulation of the perpendicular termination shock with parameters as described in Section 3. Figure 1 uses black lines to illustrate the profiles of the main component of the magnetic field $B_y(x)$ at $\Omega_i t = 60$ and at three different values of y given in the figure caption. The shock is at $x \simeq 197\lambda_i$ at this moment. This figure shows substantial variability in the magnetic profile as a function of y , just as Voyager 2 observed a variety of different profiles during its multiple crossings of the termination shock [*Burlaga et al.*, 2008]. Nevertheless, the y -averaged magnetic field, indicated by the gray line in Figure 1 and denoted as $\overline{B_y}$, exhibits the main magnetic features of a perpendicular shock, namely, the foot, ramp, and overshoot, as well as downstream oscillations along x , similar to the magnetic fluctuations computed in one-dimensional simulations [*Wu et al.*, 2009, 2010]. These downstream fluctuations decrease with increasing x faster than in the comparable one-dimensional shock simulations. This is consistent with the time-stationary (with respect to the shock) oscillations observed at a clean perpendicular shock at Earth by Cluster [*Horbury et al.*, 2001; *Bale*, 2005] and is associated with the relaxation of the downstream plasma anisotropies, which is precluded in the one-dimensional model.

Figure 2 displays y -averaged plasma properties of the solar wind ion component (left panels) and the pickup ions (right panels) as functions of x at $\Omega_i t = 60$. Panels from top to bottom present the j th ion component densities averaged over y , the component temperatures, the component temperature ratios $T_{\perp j}/T_{\parallel j} = (T_{xj} + T_{zj})/(T_{yj}/2)$, and the

component $\beta_{\parallel j}$, respectively. The temperatures here are calculated from $T_{x,y,z} = m_i < v_{x,y,z}^2 - < v_{x,y,z} >^2 >$, where the notation “ $< >$ ” means the velocity-averaged value of the enclosed quantity over all the ions of a particular component. Note that the solar wind ions and the pickup ions are not necessarily Maxwellian at places, especially in the vicinity of the shock.

Consistent with the one-dimensional results of *Wu et al.* [2009], the temperature increase of the solar wind ions across the shock (~ 50) is much larger than that of the pickup ions, but the energy gain of the pickup ions accounts for most ($> 80\%$) of the shock dissipation. Accordingly, $\beta_{\parallel sw}$ shown in Figure 2g jumps from its upstream value of 0.04 to about 0.8 across the shock associated with the significant increase of T_{swy} displayed in Figure 2c. The solar wind ions have a large anisotropy near the shock as shown by the big spike (~ 25) of T_{\perp}/T_{\parallel} of the solar wind ions in Figure 2e. This anisotropy declines to ~ 1.5 immediately downstream of the shock. Across the shock, the average $\beta_{\parallel pu}$ does not change significantly except for some oscillations associated with the changes in $\overline{B_y}$ as shown in Figure 1. The pickup ion T_{\perp}/T_{\parallel} increases to 2.5 near the shock and gradually declines to about 1.2 far downstream.

Using the plasma parameters illustrated in Figure 2, we have solved the kinetic linear dispersion equation for two locations: immediately downstream of the shock near $x/\lambda_i \simeq 197$ and somewhat further downstream near $x/\lambda_i \simeq 210$. At both locations, the Alfvén-cyclotron instabilities have appreciably faster growth rates than their proton mirror instability counterparts. Immediately downstream, theory predicts that the very strong anisotropy of the thermal component is the dominant instability driver, whereas

further downstream, after $T_{\perp t}/T_{\parallel t}$ is substantially reduced, the weaker suprathermal ion anisotropy becomes the primary driver of the Alfvén-cyclotron enhanced fluctuations.

5. Simulations: Fluctuating fields

In addition to the Alfvén-cyclotron and mirror-like fluctuations discussed in Section 2, previous simulations have demonstrated that there is a third type of fluctuating magnetic field near the shock which is not a normal mode of linear theory but corresponds to the magnetosonic-like character of the shock itself, with $|\delta B_{\parallel}|^2 \gg |\delta B_{\perp}|^2$. Such fluctuations are intrinsic to one-dimensional shock simulations [e.g., *Liewer et al.*, 1993; *Kucharek and Scholer*, 1995; *Wu et al.*, 2009], and have been demonstrated in the two-dimensional bow shock simulations of *McKean et al.* [1995]. We call these “non-modal” fluctuations, and show that they propagate primarily at $k_{\parallel} = 0$, although they have smaller amplitude oblique components as well.

Magnetic fluctuations from both the Alfvén-cyclotron and proton mirror instabilities are excited downstream of the shock in the present two-dimensional simulation as shown by Figure 3, which displays B_x , $\delta B_y = B_y - \overline{B_y}$ ($\overline{B_y}$ is subtracted away to highlight the remaining smaller amplitude fluctuations in B_y), and B_z at $\Omega_i t = 60$. The Alfvén-cyclotron modes correspond to magnetic fluctuations in B_z because the mirror mode and the non-modal fluctuations have insignificant B_z components. As shown by Figure 3c, the fluctuations in B_z have locally field-aligned wavenumbers. Near the shock, the solar wind ions have a large anisotropy (as shown in Figure 2e) and drive Alfvén-cyclotron modes at relatively short wavelengths; the resulting enhanced fluctuations rapidly reduce the driving anisotropy. Once the free energy is depleted in the thermal or solar wind component, the anisotropy on the pickup ions or suprathermals becomes the dominant driver for

the instability and the resulting enhanced fluctuations have relatively longer wavelengths (Compare Figures 11a and 11b). Far downstream of the shock, both anisotropies are relaxed and the remaining Alfvén-cyclotron fluctuations damp with x .

In Figure 3a, the fluctuations in B_x , like those in B_z , propagate at $\mathbf{k} \times \mathbf{B}_o = 0$, showing that these fluctuations are predominantly the corresponding coplanar transverse component of the Alfvén cyclotron fluctuations in B_z . In contrast, the fluctuations in δB_y of Figure 3b are very different from those in B_x and B_z . Figure 3b demonstrates large amplitude fluctuations of short scales near the shock. Further downstream, these fluctuations become weaker and demonstrate oblique propagation with longer wavelengths. Compressive modes at oblique propagation are characteristic of the proton mirror instability.

Figure 4 shows the magnetic fluctuation spectra as functions of k_y at two different x locations and at $\Omega_i t = 60$. The left panels are for magnetic fluctuations at $x = 210\lambda_i$, immediately downstream of the shock. The right panels are for magnetic fluctuations at $x = 300\lambda_i$, far downstream of the shock. From top to bottom, panels (a) and (b) present $|B_x(k_y)|^2$, panels (c) and (d) show $|\delta B_y(k_y)|^2$, and panels (e) and (f) illustrate $|B_z(k_y)|^2$. This figure shows that most wavelength fluctuations decrease with increasing x for all three magnetic components. Furthermore, the maximum fluctuating magnetic energy shifts to longer wavelengths as distance from the shock increases. However, the transverse components, $|\delta B_x(k_y)|^2$ and $|\delta B_z(k_y)|^2$, retain spectral peaks at $k_y > 0$ in the far downstream, indicating that the Alfvén-cyclotron fluctuations have maintained weak growth, whereas the $|\delta B_y(k_y)|^2$ compressive component spectrum decreases monotonically with k_y , showing that the mirror-like fluctuations are consistently damped here.

Figure 5a displays magnetic fluctuation spectra $|B_z(k_y)|^2$ at $\Omega_i t = 60$ as functions of x . Figure 5b is the same as Figure 5a but has curves superimposed on it to represent the most unstable k_y calculated from linear dispersion theory of the Alfvén-cyclotron instability using the local plasma parameters given by Figure 2 with the assumption that both ion components have bi-Maxwellian velocity distributions. The red and blue curves represent instabilities driven by anisotropies of the solar wind ions and the pickup ions, respectively (See the Appendix). The dashed part of each curve means that the growth rate of the corresponding mode is smaller than that of the other mode. The most intense wavenumbers from the simulation agree with the linear theory prediction reasonably well, confirming our interpretation that the enhanced fluctuations in B_z are generated by the Alfvén-cyclotron instability.

Figure 6 presents a two-dimensional spectral analysis of the magnetic fluctuations over $200\lambda_i < x < 300\lambda_i$ at $\Omega_i t = 60$. Panels a), b), c), and d) display spectra of B_x , B_y (with the areal average of B_y subtracted away), B_z and $\delta B_y = B_y - \overline{B_y}$, respectively. Here $|B_x(k_x, k_y)|^2$ and $|B_z(k_x, k_y)|^2$ are similar and further confirm the field-aligned propagation feature of these fluctuations. The dominant fluctuations clearly have $k_x = 0$ and $0.15 < k_y \lambda_i < 0.50$, consistent with the linear dispersion theory prediction for Alfvén-cyclotron waves as shown in Figure 5b. The spectrum of B_y in Figure 6b has dominating fluctuations with $k_y = 0$, which are the features of non-modal fluctuations demonstrated by previous one-dimensional simulations of perpendicular and quasi-perpendicular shocks. But there are also relatively weak oblique fluctuations with nonzero k_y ($k_y \lambda_i \approx 0.1$) in $|B_y(k_x, k_y)|^2$, which do not show up very well due to the dominance of the $k_y = 0$ fluctuations. These oblique fluctuations stand out in Figure 6d after the $k_y = 0$ fluctuations

are removed subtracting $\overline{B_y}$ from B_y before the spectral analysis. As discussed below, these oblique fluctuations are a combination of the mirror modes and some oblique non-modal fluctuations. From $\nabla \cdot \mathbf{B} = 0$, there should be B_x fluctuations in the present two-dimensional simulation associated with these oblique fluctuations in B_y . This is indeed the case as shown by the oblique fluctuation in Figure 6a, which is at the same location ($k_x \lambda_i \approx 0.1$, $k_y \lambda_i \approx 0.08$) as the strongest fluctuation in Figure 6d.

In order to identify the oblique fluctuations in Figure 6d, the correlation coefficient between $\delta B_y = B_y - \overline{B_y}$ and the density fluctuations $\delta n_i = n_i - \overline{n_i}$ [similar to $\overline{B_y}$, $\overline{n_i}$ is $n_i(x, y)$ averaged over y] as a function of x is displayed in Figure 7. The density fluctuations are rather noisy due to limited number of particles per cell, so this coefficient exhibits rather large amplitude oscillations. Nevertheless, it is clear that the correlation coefficient is close to 1 near the shock, decreases rapidly thereafter, and displays small but negative values farther downstream of the shock. Near the shock, the density fluctuations and the magnetic fluctuations are positively correlated, indicative of the basic magnetosonic character of the shock. Farther downstream, the negative correlation between the density fluctuations and the magnetic fluctuations further confirms our interpretation that mirror-like fluctuations are present here.

Figure 8 displays magnetic fluctuation component energy densities $\overline{B_x^2}$ (red curve), $\overline{\delta B_y^2}$ (black curve), and $\overline{B_z^2}$ (blue curve) versus x . The energy in B_z , which indicates the development of Alfvén-cyclotron modes, grows quickly after the shock, reaches saturation and then decreases farther downstream. This is consistent with the picture that these fluctuations are generated through the Alfvén-cyclotron instability driven by the anisotropies in both ion components as shown in Figure 2 and as indicated by the linear theory of

the Appendix. The first maximum at $x = 200\lambda_i$ in $\overline{B_z^2}$ is due to the short-wavelength modes driven by the solar wind ion anisotropy. These modes decrease thereafter while the longer wavelength modes driven by the pickup ions still increase and reach a maximum amplitude at $x = 215\lambda_i$. The $\overline{B_x^2}$ demonstrates similar behavior as $\overline{B_z^2}$ suggesting once again that the contributions of the mirror modes and the non-modal fluctuations in B_x are small compared with those of the Alfvén-cyclotron mode.

However, the compressive component of the magnetic spectrum behaves differently than the other two and reaches a large maximum right at the shock overshoot. Our interpretation is that this maximum is due to the non-modal fluctuations as suggested by Figure 7. The oblique non-modal fluctuations decay quickly as one goes downstream, but have strong coupling to the mirror-like fluctuations at the shock, which persist deeper into the downstream. This is different from the Alfvén-cyclotron fluctuations, which have to grow from relatively small amplitude initial perturbations in B_x and B_z , and explains why the amplitude of the mirror mode fluctuations are relatively large compared to what might be expected from predictions of linear dispersion theory. The energy of the mirror mode fluctuations reaches its maximum at $215\lambda_i$ as well, where the large pickup ion anisotropy ceases. After that, both the Alfvén-cyclotron and mirror mode fluctuations decrease while the Alfvén-cyclotron fluctuations damp slightly slower, consistent with the linear dispersion theory prediction that the Alfvén cyclotron instability has a smaller anisotropy threshold than the mirror instability given the local plasma parameters from Figure 2. At $x = 300\lambda_i$, the energy of the Alfvén-cyclotron fluctuations is $\overline{B_x^2} + \overline{B_z^2} \approx 0.2$ while the energy of the mirror mode fluctuations is $\leq \overline{\delta B_y^2} \approx 0.04$. Thus the Alfvén-cyclotron mode dominates the mirror mode sufficiently far downstream from the shock, although

the mirror mode is much stronger than one might expect from the predictions of linear dispersion theory.

The primary consequence of wave-particle interactions by the dominant Alfvén-cyclotron fluctuations is ion pitch-angle scattering, so that the high-speed part of suprathermal ion perpendicular velocity distributions in the heliosheath should be depleted by comparison with those computed from one-dimensional hybrid simulations. This is demonstrated in Figure 9, which compares the downstream perpendicular ion velocity distributions at $\Omega_i t = 60$ from one-dimensional and two-dimensional simulations with the same upstream conditions. Both distributions are obtained by directly binning ions in their respective speed space. This figure shows clearly that suprathermal ions at $v_\perp > 10v_A$ are depleted, whereas suprathermals at $v_\perp \leq 10v_A$ are enhanced, consistent with the physical picture of ion pitch-angle scattering by Alfvén-cyclotron fluctuations.

6. Summary and Conclusions

This paper has described a two-dimensional, zero-electron-mass hybrid simulation of the perpendicular termination shock. This simulation generalizes the one-dimensional computations of *Wu et al.* [2009, 2010], and demonstrates properties of the enhanced fluctuations which arise in the heliosheath.

Analysis of our simulation shows three distinct types of fluctuations at and downstream of the shock: Alfvén-cyclotron modes, mirror-like modes, and “non-modal” fluctuations. The first two of these correspond to normal modes which can be described by linear dispersion theory in the relatively uniform downstream plasma, whereas the non-modal fluctuations are intrinsically nonlinear oscillations associated with the strong inhomogeneities at and near the shock. The Alfvén-cyclotron fluctuations have magnetic fluctuations primar-

ily perpendicular to the background magnetic field \mathbf{B}_o , $|\delta B_\perp|^2$, whereas both the mirror
 fluctuations and the non-modal fluctuations are strongly compressive, with $|\delta B_\parallel|^2$ dom-
 inating the magnetic fluctuation energy. Mirror-like fluctuations have anticorrelated δn
 and δB_\parallel , whereas the magnetosonic-like non-modal fluctuations have positively correlated
 density and compressive magnetic fluctuations.

We interpret the downstream enhanced fluctuations in our simulation as follows. The
 primary driver of the mirror-like fluctuations is their coupling to the compressive mag-
 netic component of the non-modal fluctuations near the shock. Thus Figure 8 shows an
 almost-monotonic decay of $|\delta B_\parallel|^2$ as x increases downstream away from the shock. The
 Alfvén-cyclotron downstream fluctuations are driven partially by coupling to the weaker
 transverse magnetic component of the non-modal fluctuations, but more strongly through
 instabilities excited by the ion component temperature anisotropies at the shock (as il-
 lustrated in Figure 2). Immediately downstream of the shock, the instability is driven
 by the thermal component $T_{\perp t}/T_{\parallel t} \gg 1$ (Figure 10a); the corresponding wavelength is
 quite short (Figure 11a). After rapid reduction of the thermal component anisotropy,
 the weaker $T_{\perp s}/T_{\parallel s} > 1$ remains and drives a weaker instability (Figure 10b) at a longer
 wavelength (Figure 11b). Thus the relatively constant magnitude of $|\delta B_{\perp\perp}|^2$ over 200
 $\lesssim x/\lambda_i \lesssim 250$ in Figure 8 indicates a competition between the decay of modes driven
 at the shock and the growth of fluctuations driven by the Alfvén-cyclotron instability.

Well downstream of the shock, our simulation further shows that Alfvén-cyclotron fluc-
 tuations have substantially larger amplitudes than mirror-like fluctuations. This is con-
 sistent with low-Mach low- β bow shock results, both simulated [McKean *et al.*, 1996]
 and observed [Schopke *et al.*, 1990]. However, high Alfvén-Mach bow shock results, both

simulated *McKean et al.* [1995] and observed [*Sckopke et al.*, 1990], show that transverse and compressive magnetic fluctuations have similar downstream amplitudes.

We here offer a hypothesis to explain these results. The intrinsic non-modal fluctuations at perpendicular and quasi-perpendicular shocks have both a strong δB_{\parallel} component and a significant k_{\perp} component. Therefore, they couple strongly to mirror-like fluctuations (which also have significant δB_{\parallel} and k_{\perp} components) and directly excite those modes via nonlinear interactions. The Alfvén-cyclotron fluctuations with $\delta B_{\parallel} = 0$ and $k_{\perp} = 0$ do not couple as strongly to the non-modal oscillations; they are more likely to arise via the development of $T_{\perp i}/T_{\parallel i} > 1$ at the shock and the subsequent linear growth of the Alfvén-cyclotron instabilities downstream. Our hypothesis is that the nonlinear excitation of mirror-like fluctuations increases more rapidly with magnetosonic Mach number than does the linear growth of the Alfvén-cyclotron instability. Thus the high Alfvén-Mach bow shock simulations of *McKean et al.* [1995] shows the two modes develop similar amplitudes downstream, whereas Alfvén-cyclotron modes dominate low Alfvén-Mach bow shock simulations [*McKean et al.*, 1996]. Although our termination shock simulation is run at $M_A = 8$, it is of course the magnetosonic Mach number which determines the strength of a perpendicular shock; as $M_{ms} < 4$ here due to the high- β contribution of the pickup ions, our hypothesis is consistent with Alfvén-cyclotron modes dominating the downstream fluctuations. Further two-dimensional simulations of the termination shock at various Alfvén-Mach numbers and with various pickup ion upstream densities will be needed to test this idea more fully.

Thus we conclude that the enhanced fluctuations of the near-shock heliosheath should consist primarily of Alfvén-cyclotron modes. We further conclude that the consequences

of wave-particle interactions in this region should be primarily pitch-angle scattering of relatively fast suprathermal ions, as indicated by Figure 9.

Observations of the heliosheath magnetic field by Voyager 1 and 2 [Burlaga *et al.*, 2005, 2008] show that the field fluctuations tend to be large amplitude, widely varying and very complex. There are indications of the presence of magnetic holes [Burlaga *et al.*, 2007] which could be signatures of mirror waves [Winterhalter *et al.*, 1994; Zhang *et al.*, 2008], but identification of individual wave modes in the Voyager data is very difficult. Instead, statistical methods have been used to characterize the distribution of magnetic field amplitudes in the heliosheath [Burlaga *et al.*, 2009]. Detailed measurements of the magnetic field strength as Voyager 2 crossed the termination shock (e. g., the crossing termed TS-3) [Burlaga *et al.*, 2008] and entered the heliosheath show the jump in the field at the shock and the fluctuations just downstream of the shock, which are generally consistent with the simulation results in Figure 1, but corresponding wave spectra are not available for more detailed comparison. The Alfvén-cyclotron and mirror modes expected downstream of the shock scatter ions differently, and their relative amplitudes in the heliosheath affect the consequent ENA fluxes which emanate from this region. However, a detailed comparison of the scattering consequences of these two modes is beyond the purview of this manuscript.

We emphasize that our conclusions are based upon a two-dimensional simulation model of the perpendicular termination shock. Two natural extensions of this work would be to consider the more general quasi-perpendicular shocks and fully three-dimensional simulations. In particular the three-dimensional computations of Shoji *et al.* [2009] suggest

that compressible mirror-like fluctuations may persist deeper into the downstream than the incompressible Alfvén-cyclotron fluctuations.

Appendix A: Linear Theory

This Appendix describes results obtained from the kinetic linear dispersion equation for waves and instabilities in a homogeneous, collisionless, magnetized plasma [Gary, 1993]. We here use linear theory to compute growth rates for instabilities driven by the anisotropy $T_{\perp j}/T_{\parallel j} > 1$ on the thermal and suprathermal ion components downstream of the termination shock. The theory is based upon the assumption that both components can be represented as bi-Maxwellian velocity distributions. Observations [Funsten *et al.*, 2009], models [Zank *et al.*, 2010 and references therein], and termination shock simulations [Wu *et al.*, 2010] all indicate that suprathermal ion velocity distributions may have power-law velocity dependence at relatively large speeds. Nevertheless, we argue that, because we are computing the growth rates of strongly resonant kinetic instabilities, it is the properties of the mid-velocities of a component distribution, not the high-velocity tails, which are most important for determining instability properties, in which case the use of bi-Maxwellian distributions is likely to be an appropriate approximation.

We use parameters from the hybrid simulations described in section 4 [See also Table 2 of Wu *et al.*, 2009] for two cases corresponding to immediately downstream and well downstream of the shock. In both cases the proton component anisotropies lead to the growth of two distinct instabilities: the Alfvén-cyclotron instability with maximum growth at $\mathbf{k} \times \mathbf{B}_o = 0$ and $0 < \omega_r < \Omega_p$, and the proton mirror instability with $\omega_r = 0$ and maximum growth rate at propagation oblique to \mathbf{B}_o .

For a strictly perpendicular shock, there is no parallel heating of the plasma, so immediately downstream we take $\beta_{\parallel t} = 0.04$ and estimate $T_{\parallel s}/T_{\parallel t} = 800.0$ as well as $T_{\perp s}/T_{\parallel s} = 2.5$, consistent with the results of the simulations described in Section 4. We assume the electrons are isotropic and $T_{\parallel e}/T_{\parallel t} = 1.0$. With these parameters, we compute the maximum growth rate γ_m/Ω_p and the corresponding wavenumber $k_m c/\omega_i$ and angle of propagation θ_m as functions of the thermal component anisotropy, with results illustrated in Figures 10a through 12a.

If the thermal component anisotropy is relatively weak, both instabilities are driven by the suprathermal anisotropy; for these parameters the Alfvén-cyclotron instability has the consistently larger value of γ_m/Ω_p . As $T_{\perp t}/T_{\parallel t}$ increases, the growth rates of the modes driven by this thermal component anisotropy also increase, and their contributions appear on the right-hand sides of the figures. For our parameters, the Alfvén-cyclotron suprathermal instability has maximum growth rate at $0.25 < k_{\parallel} c/\omega_p < 0.30$, but the Alfvén-cyclotron thermal mode has maximum growth at $k_{\parallel} c/\omega_p > 1$. Similarly, the suprathermal mirror instability has γ_m at $kc/\omega_p \simeq 0.185$ while the thermal mirror mode has maximum growth at $kc/\omega_p > 1$. Figure 12a shows that θ_m of the suprathermal mirror instability is a weak function of the thermal proton anisotropy, but that the thermal mirror instability propagates at successively steeper angles with respect to \mathbf{B}_o as $T_{\perp t}/T_{\parallel t}$ decreases and the instability is correspondingly weakened.

The simulations demonstrate that a short distance downstream of the shock, the thermal protons are scattered to near-isotropy. For our calculations in this second regime, we assume $T_{\perp t}/T_{\parallel t} = 1.5$, $T_{\parallel s}/T_{\parallel t} = 30.0$, and $\beta_{\parallel t} = 0.80$. Using these parameters, we plot in Figure 10b the maximum growth rates of the Alfvén-cyclotron and mirror insta-

bilities driven by the suprathermal component anisotropy as a function of $T_{\perp s}/T_{\parallel s}$. Once again, the Alfvén-cyclotron mode has the consistently higher growth rate, so that we expect this mode to dominate magnetic field fluctuations in the far downstream, in agreement with the simulations described above. Figure 11b shows that the Alfvén-cyclotron instability here has a relatively long wavelength, with $0.10 < k_{\parallel}c/\omega_p < 0.30$ at maximum growth. Figure 12b shows that the angle of propagation at maximum growth rate of the suprathermal mirror instability becomes more nearly perpendicular to \mathbf{B}_o as the suprathermal anisotropy decreases and the instability weakens.

Acknowledgments. This work was performed under the auspices of the U.S. Department of Energy (DOE). It was supported by the Solar and Heliospheric Physics SR&T Program of the National Aeronautics and Space Administration.

References

- Anderson, B. J., S. A. Fuselier, S. P. Gary, and R. E. Denton (1994) Magnetic spectral signatures in the Earth’s magnetosheath and plasma depletion layer, *J. Geophys. Res.*, *99*, 5877.
- Bale, S. (2005), Quasi-perpendicular shock structure and processes, *Space Sci. Rev.*, *118*, 161–203.
- Burlaga, L. F., N. F. Ness, M. H. Acuña, R. P. Lepping, J. E. P. Connerney, E. C. Stone, and F. B. McDonald (2005), Crossing the termination shock into the heliosheath: Magnetic fields, *Science*, *309*, 2027.
- Burlaga, L. F., N. F. Ness, and M. H. Acuña (2007), Linear magnetic holes in a unipolar region of the heliosheath observed by Voyager 1, *J. Geophys. Res.*, *112*, A07106.

- Burlaga, L. F., N. F. Ness, M. H. Acuña, R. P. Lepping, J. E. P. Connerney, and J. D. Richardson (2008), Magnetic fields at the solar wind termination shock, *Nature*, *454*, 75.
- Burlaga, L. F., N. F. Ness, M. H. Acuña, J. D. Richardson, E. Stone, and F. B. McDonald (2009), Observations of the heliosheath and solar wind near the termination shock by Voyager 2, *Astrophys. J.*, *692*, 1125.
- Chapman, S. C., R. E. Lee, and R. O. Dendy (2005), Perpendicular shock reformation and ion acceleration, *Space Sci. Revs.*, *121*, 5.
- Farrugia, C. J., F. T. Gratton, G. Gnani, H. Matsui, R. B. Torbert, D. H. Fairfield, K. W. Ogilvie, R. P. Lepping, T. Terasawa, T. Mukai, and Y. Saito (2005), Magnetosheath waves under very low solar wind dynamic pressure: Wind/Geotail observations, *Ann. Geophys.*, *23*, 1317.
- Funsten, H. O., *et al.* (2009), Structures and spectral variations of the outer heliosphere in IBEX energetic neutral atom maps, *Science*, *326*, 964.
- Gary, S. P. (1992), The mirror and ion cyclotron anisotropy instabilities, *J. Geophys. Res.*, *97*, 8519.
- Gary, S. P. (1993), *Theory of space plasma microinstabilities*, Cambridge Univ. Press, New York.
- Giacalone, J., and R. Decker (2010), The origin of low-energy anomalous cosmic rays at the solar-wind termination shock, *Astrophys. J.*, *710*, 91.
- Greenstadt, E. W., C. T. Russell, J. T. Gosling, S. J. Bame, G. Pashchmann, G. K. Parks, K. A. Anderson, F. L. Scarf, R. R. Anderson, D. A. Gurnett, R. P. Lin, C. S. Lin, and H. Réme (1980), A macroscopic profile of the typical quasi-perpendicular bow shock:

564 ISEE 1 and 2, *J. Geophys. Res.*, *85*, 2124.

565 Horbury, T. S., P. Cargill, E. A. Lucek, A. Balogh, M. W. Dunlop, T. M. Oddy, C. Carr,
566 P. Brown, A. Szabo, and K.-H. Fornacon (2001), Cluster magnetic field observations of
567 the bowshock: Orientation, motion and structure, *Ann. Geophys.*, *19*, 1399–1409.

568 Kucharek, H., and M. Scholer (1995), Injection and acceleration of interstellar pickup ions
569 at the heliospheric termination shock, *J. Geophys. Res.*, *100*, 1745.

570 Lee, R. E., S. C. Chapman, and R. O. Dendy (2005), Reforming perpendicular shocks in
571 the presence of pickup protons: Initial ion acceleration, *Ann. Geophys.*, *23*, 643.

572 Liewer, P. C., B. Goldstein, and N. Omid (1993), Hybrid simulations of the effects of
573 interstellar pickup hydrogen on the solar wind termination shock, *J. Geophys. Res.*,
574 *98*(A9), 15,211.

575 Liewer, P. C., S. Rath, and B. E. Goldstein (1995), Hybrid simulations of interstellar
576 pickup ion acceleration at the solar wind termination shock, *J. Geophys. Res.*, *100*,
577 19,809.

578 Matsukiyo, S., M. Scholer, and D. Burgess (2007), Pickup protons at quasi-perpendicular
579 shocks: Full particle electrodynamic simulations, *Ann. Geophys.*, *25*, 283.

580 McComas, D. J., et al. (2004), The Interstellar Boundary Explorer (IBEX), in Physics of
581 the Outer Heliosphere, 719, 162, Edited by V. Florinski, N. V. Pogorelov, and G. P.
582 Zank, Am. Inst. of Phys., Melville, NY.

583 McComas, D. J. *et al.* (2009), Global observations of the interstellar interaction from the
584 Interstellar Boundary Explorer (IBEX), *Science*, *326*, 959.

585 McKean, M. E., D. Winske, and S. P. Gary (1992), Mirror and ion cyclotron anisotropy
586 instabilities in the magnetosheath, *J. Geophys. Res.*, *97*(A12), 19,421.

- McKean, M. E., D. Winske, and S. P. Gary (1994), Two-dimensional simulations of ion anisotropy instabilities in the magnetosheath, *J. Geophys. Res.*, *99*, 11,141.
- McKean, M. E., N. Omidi, and D. Krauss-Varban (1995), Wave and ion evolution downstream of quasi-perpendicular bow shocks, *J. Geophys. Res.*, *100*(A3), 3427.
- McKean, M. E., N. Omidi, and D. Krauss-Varban (1996), Magnetosheath dynamics downstream of low Mach number shocks, *J. Geophys. Res.*, *101*, 20,013.
- Scholer, M., H. Kucharek, and C. Kato (2002), On ion injection at quasiparallel shocks, *Phys. Plas.*, *9*, 4293.
- Sckopke, N., G. Paschmann, A. L. Brinca, C. W. Carlson, and H. Lühr (1990), Ion thermalization in quasi-perpendicular shock involving reflected ions, *J. Geophys. Res.*, *95*, 6337.
- Shoji, M., Y. Omura, B. T. Tsurutani, O. P. Verkhoglyadova, and B. Lembege (2009), Mirror instability and L-mode electromagnetic ion cyclotron instability: Competition in the Earth's magnetosheath, *J. Geophys. Res.*, *114*, A10203.
- Stone, E. C., A. C. Cummings, F. B. McDonald, B. C. Heikkila, N. Lal, and W. R. Webber (2005), Voyager 1 explores the termination shock region and the heliosheath beyond, *Science*, *309*, 2017.
- Stone, E. C., A. C. Cummings, F. B. McDonald, B. C. Heikkila, N. Lal, and W. R. Webber (2008), An asymmetric solar wind termination shock, *Nature*, *454*, 71.
- Thomas, V. A. (1989), Dimensionality effects in hybrid simulations of high Mach number collisionless perpendicular shocks, *J. Geophys. Res.*, *94*, 12,009.
- Thomas, V. A., and S. H. Brecht (1986), Two-dimensional simulation of high Mach number plasma interactions, *Phys. Fluids*, *29*, 2444.

- 610 Thomas, V. A., and S. H. Brecht (1987), Angular dependence of high Mach number
611 plasma interactions, *J. Geophys. Res.*, *92*, 3175.
- 612 Vasyliunas, V. M., and G. L. Siscoe (1976), On the flux and energy spectrum of interstellar
613 ions in the solar system, *J. Geophys. Res.*, *81*, 1247.
- 614 Winske, D., and S. P. Gary (2007), Hybrid simulations of debris-ambient ion interactions
615 in astrophysical explosions, *J. Geophys. Res.*, *112*, A10303, doi:10.1029/-2007JA012276.
- 616 Winske, D., and N. Omid (1993), Hybrid codes: Methods and applications, in *Computer*
617 *Space Plasma Physics: Simulation Techniques and Software*, edited by H. Matsumoto
618 and Y. Omura, p. 103, Terra Scientific, Tokyo.
- 619 Winske, D., and N. Omid (1996), A nonspecialist's guide to kinetic simulations of space
620 plasmas, *J. Geophys. Res.*, *101* (A8), 17,287.
- 621 Winske, D., and K. Quest (1988), Magnetic field and density fluctuations at perpendicular
622 supercritical collisionless shocks, *J. Geophys. Res.*, *93*(A9), 9681–9693.
- 623 Winske, D., L. Yin, N. Omid, H. Karimabadi and K. B. Quest (2003), Hybrid codes:
624 Past, Present and Future, in *Space Plasma Simulation*, edited by J. Buechner, C. T.
625 Dum and M. Scholer, Springer Verlag, pp. 140-169.
- 626 Winterhalter, D., M. Neugebauer, B. E. Goldstein, E. J. Smith, S. J. Bame, and A. Balogh
627 (1994), Ulysses field and plasma observations of magnetic holes in the solar wind and
628 their relation to mirror-mode structures, *J. Geophys. Res.*, *99*, 23,371.
- 629 Wu, P., D. Winske, S. P. Gary, N. A. Schwadron, and M. A. Lee (2009), Energy dissipation
630 and ion heating at the heliospheric termination shock, *J. Geophys. Res.*, *114*(A08103),
631 doi:10.1029/2009JA014240.

- Wu, P., D. Winske, S. P. Gary, N. A. Schwadron, H. O. Funsten, and K. Liu (2010),
Hybrid simulations of the termination shock: Suprathermal ion velocity distributions
in the heliosheath, *J. Geophys. Res.*, in press.
- Yin, L., D. Winske, W. Daughton, and F. V. Coroniti (2005), Dissipation in oblique slow
shocks, *J. Geophys. Res.*, 110, A09217.
- Zank, G. P., H. L. Pauls, I. H. Cairns, and G. M. Webb (1996), Interstellar pickup ions and
quasi-perpendicular shocks: Implications for the termination shock and interplanetary
shocks, *J. Geophys. Res.*, 101, 457.
- Zank, G. P., J. Heerikhuisen, N. V. Pogorelov, R. Burrows, and D. McComas (2010),
Microstructure of the heliospheric termination shock: Implications for energetic neutral
atom observations, *Astrophys. J.*, 708, 1092.
- Zhang, T. L. *et al.* (2008), Characteristic size and shape of the mirror mode structures in
the solar wind at 0.72 AU, *Geophys. Res. Lett.*, 35, L10106.

Figure 1. B_y profiles at simulation time $\Omega_i t = 60$ and different y -values (black lines): (a) $y = 50\lambda_i$, (b) $y = 125\lambda_i$, and (c) $y = 200\lambda_i$. The gray line in each panel is B_y averaged over y ($\overline{B_y}$).

Figure 2. Plasma properties of the solar wind ions (left column) and pickup ions (right column) as functions of x at simulation time $\Omega_i t = 60$. The panels present, in succession from top to bottom, the ion component density averaged over y and normalized to the upstream total plasma density, the ion component temperatures normalized to the average upstream value of $m_i v_A^2$ where $T_j = m_i \langle v_j^2 \rangle - \langle v_j \rangle^2$ and $\langle \rangle$ represents a velocity average over the ion component j (T_x , T_y , and T_z are represented by red, black, and blue lines, respectively), the component temperature ratio $T_{\perp j}/T_{\parallel j} = (T_{xj} + T_{zj})/(T_{yj}/2)$, and the ion component $\beta_{\parallel j}$.

Figure 3. The magnetic fluctuations excited downstream of the shock at simulation time $\Omega_i t = 60$: (a) $B_x(x, y)$, (b) $\delta B_y(x, y) = B_y(x, y) - \overline{B_y(x, y)}$ and (c) $B_z(x, y)$.

Figure 4. Spectra of magnetic fluctuations as functions of k_y at two x locations and at simulation time $\Omega_i t = 60$. The left panels are at $x = 210\lambda_i$, immediately downstream of the shock. The right panels are at $x = 300\lambda_i$, far downstream of the shock. The panels from top to bottom present the spectra of $|B_x(k_y)|^2$ (panels a and b), $|\delta B_y(k_y)|^2$ (panels c and d), and $|B_z(k_y)|^2$ (panels e and f), respectively.

Figure 5. (a) The spectra $|B_z(k_y)|^2$ at simulation time $\Omega_i t = 60$ as a function of x . (b) Same as (a), but with curves superimposed to represent the most unstable k_y calculated from linear dispersion theory of the Alfvén-cyclotron instability using the local plasma parameters given by Figure 2. The red curve and the blue curve are for modes driven by the anisotropies of the solar wind and pickup ions, respectively. The dashed part of each curve means that the growth rate of the corresponding mode is smaller than the growth rate of the other mode.

Figure 6. Two-dimensional wavenumber spectra of the three components of magnetic fluctuations over $200\lambda_i < x < 300\lambda_i$ at simulation time $\Omega_i t = 60$: (a) $|B_x(k_x, k_y)|^2$, (b) $|B_y(k_x, k_y)|^2$ (with the areal average of B_y subtracted away), (c) $|B_z(k_x, k_y)|^2$, and (d) $|\delta B_y(k_x, k_y)|^2$.

Figure 7. The correlation coefficient between $\delta B_y = B_y - \overline{B_y}$ and density fluctuations $\delta n_i = n_i - \overline{n_i}$ as a function of x .

Figure 8. Magnetic fluctuation component energies as functions of x at simulation time $\Omega_i t = 60$. Here the red curve indicates $\overline{B_x^2}$, the black curve indicates $\overline{\delta B_y^2}$ and the blue curve denotes $\overline{B_x^2}$.

Figure 9. Ion perpendicular velocity distributions $v_\perp f(v_\perp)$ downstream of the shock summed over all y values and $250 \leq x/\lambda_i \leq 350$ at simulation time $\Omega_i t = 60$ from a one-dimensional simulation (dashed line) and from the two-dimensional simulation (solid line).

Figure 10. Linear theory results: The maximum growth rates of Alfvén-cyclotron (solid lines) and proton mirror (dashed lines) instabilities from kinetic linear dispersion theory. For both panels, $n_s/n_o = 0.20$. (a) Maximum growth rates as a function of the thermal proton component anisotropy. Parameters here are characteristic of those immediately behind a termination shock: $\beta_{\parallel t} = 0.04$, $T_{\parallel s}/T_{\parallel t} = 800.0$ and $T_{\perp s}/T_{\parallel s} = 2.5$. The left-hand, relatively horizontal lines represent instabilities driven by the suprathermal ion anisotropy, whereas the right-hand, upward trending lines represent instabilities driven by the thermal ion anisotropy. (b) Maximum growth rates of instabilities driven by the suprathermal proton anisotropy, as functions of that anisotropy. Parameters here are characteristic of those somewhat downstream of a termination shock: $\beta_{\parallel t} = 0.80$, $T_{\parallel s}/T_{\parallel t} = 30.0$ and $T_{\perp t}/T_{\parallel t} = 1.5$.

Figure 11. Linear theory results: The dimensionless wavenumbers at maximum growth rates of the Alfvén-cyclotron (solid lines) and proton mirror (dashed lines) instabilities from kinetic linear dispersion theory. Parameters are the same as for the corresponding panels in Figure 10. (a) Wavenumbers as functions of the thermal proton anisotropy. The upper two curves correspond to instabilities driven by the thermal proton anisotropy, whereas the lower two curves represent wavenumbers of instabilities driven by the suprathermal proton anisotropy. (b) Wavenumbers of the instabilities driven by the suprathermal proton anisotropy as functions of that anisotropy.

Figure 12. Linear theory results: The angle at maximum growth rate θ_m of the proton mirror instabilities from kinetic linear dispersion theory. Parameters are the same as for the corresponding panels in Figure 10. (a) Values of θ_m as functions of the thermal proton anisotropy, corresponding to the two different types of mirror instability as labeled. (b) Values of θ_m of the suprathermal mirror instability as a function of the suprathermal anisotropy.

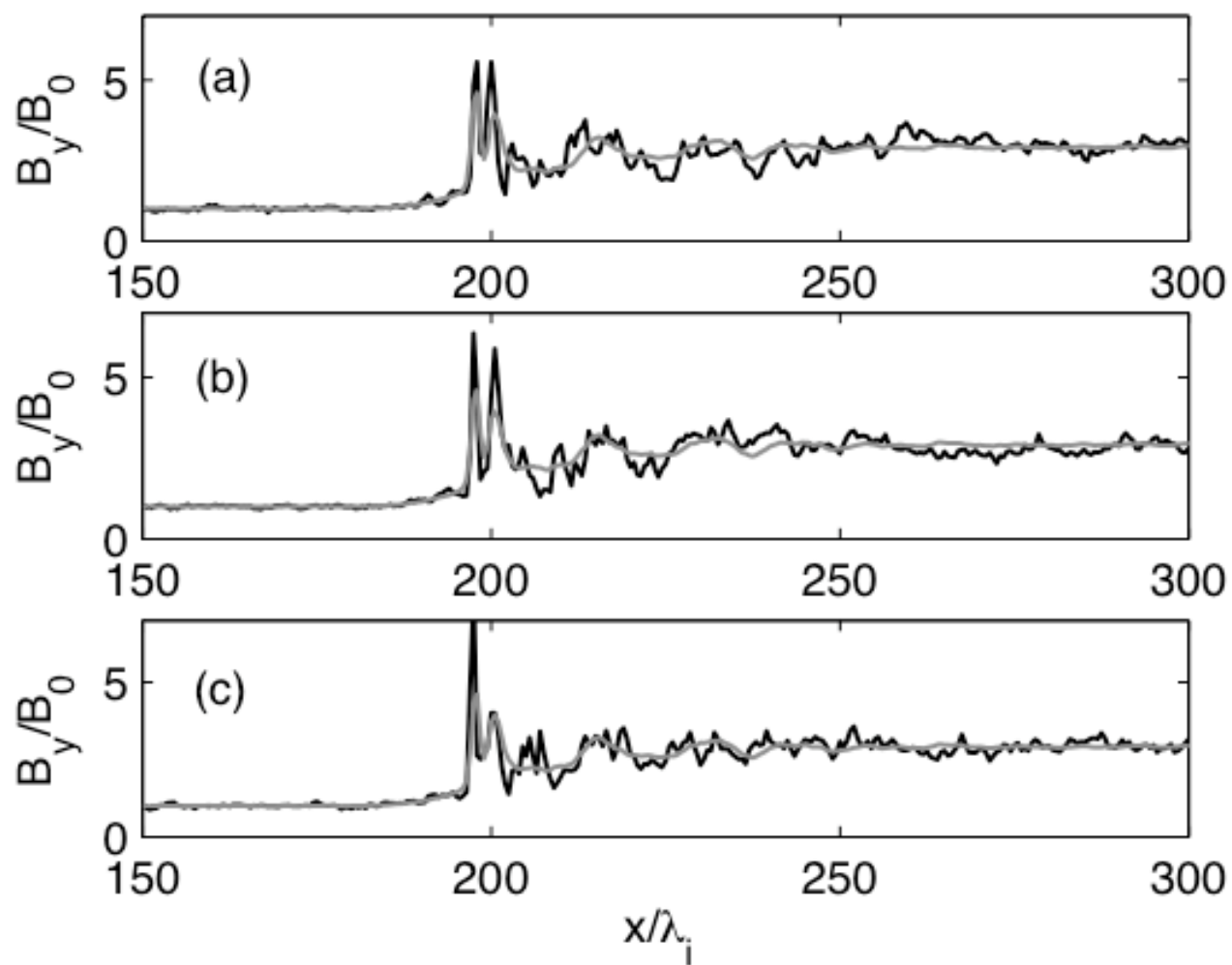


Figure 1

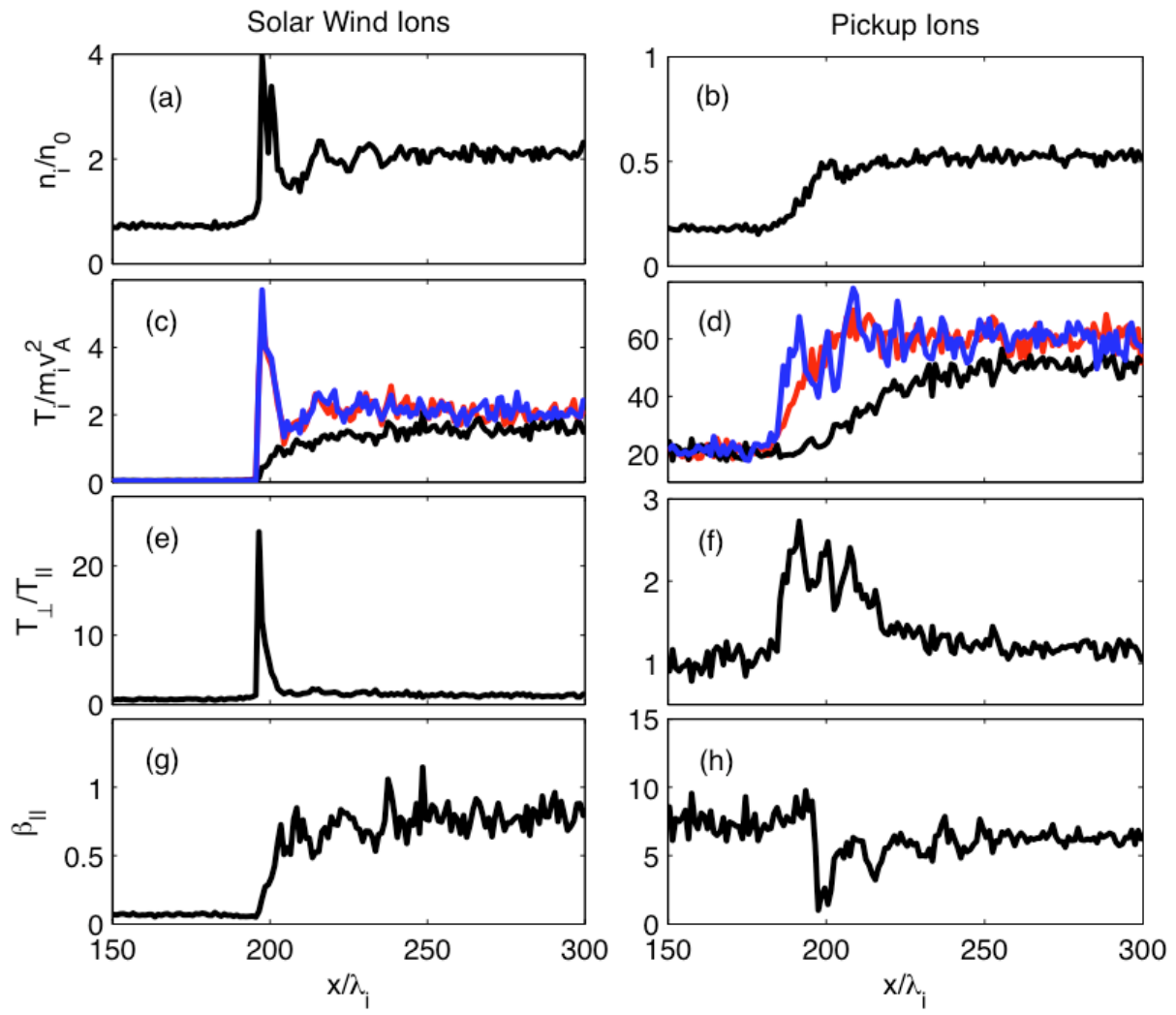


Figure 2

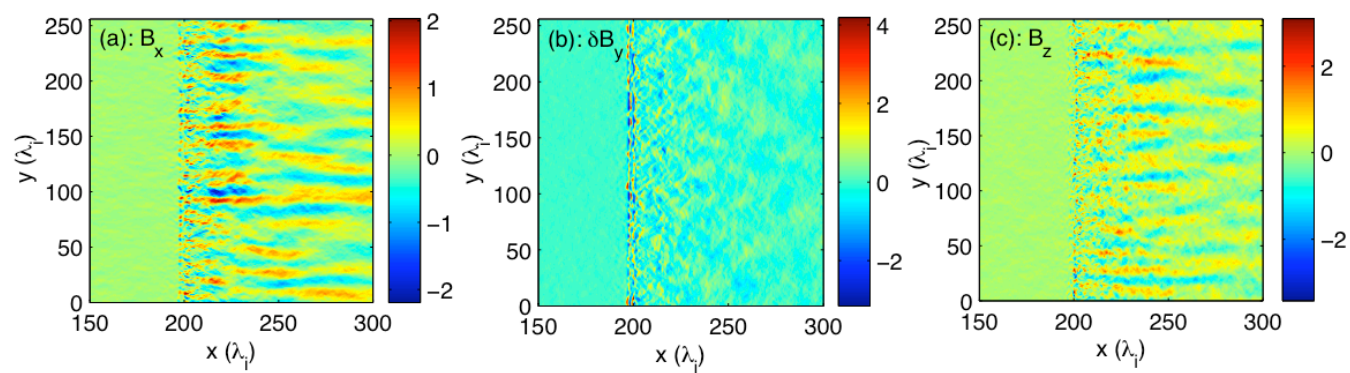


Figure 3

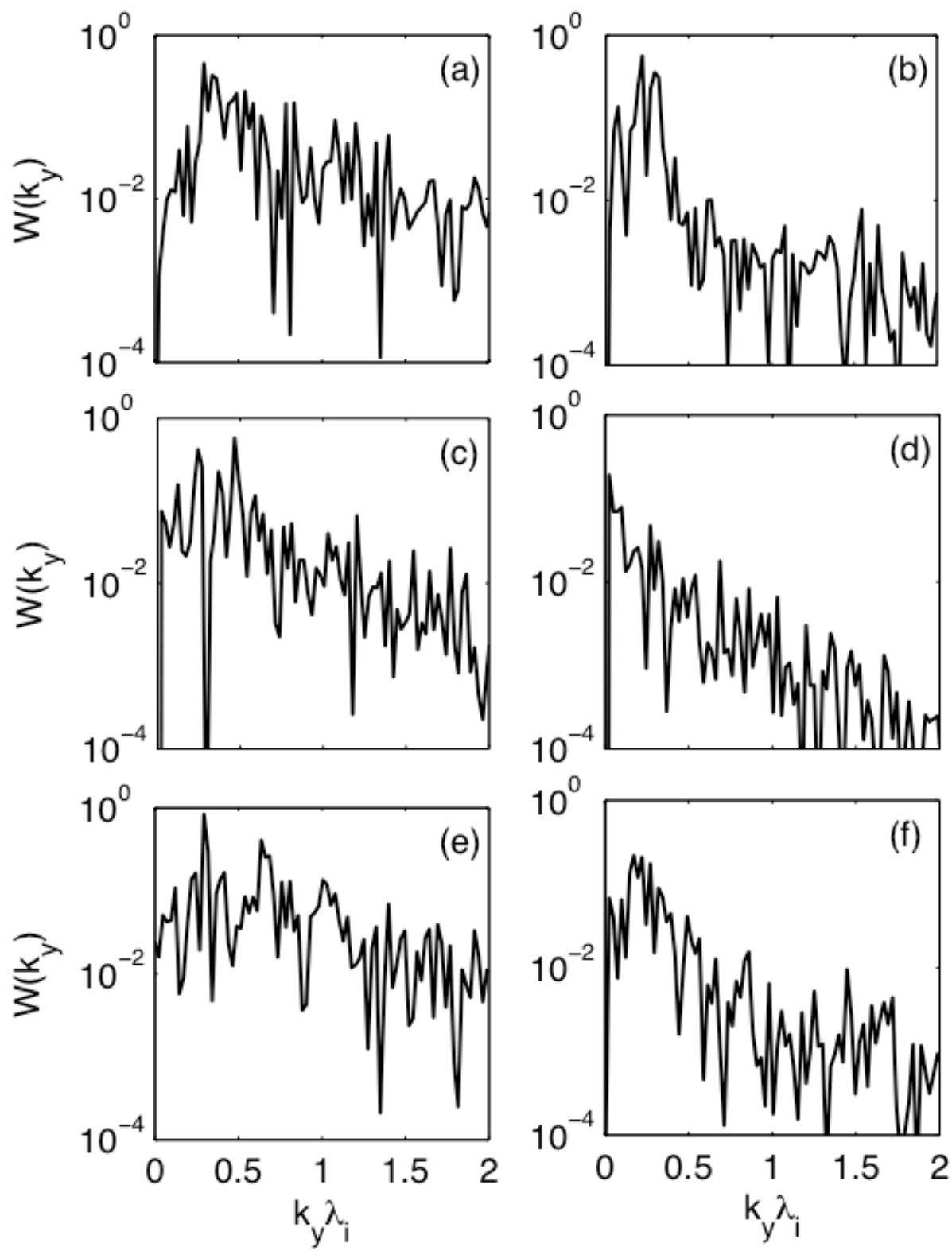


Figure 4

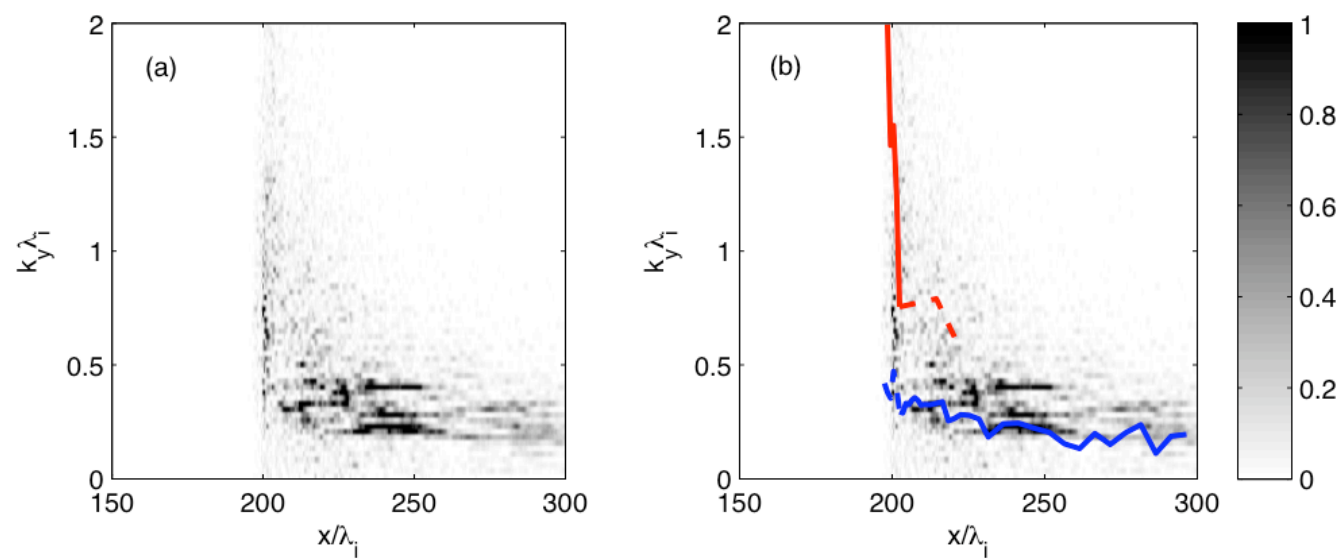


Figure 5

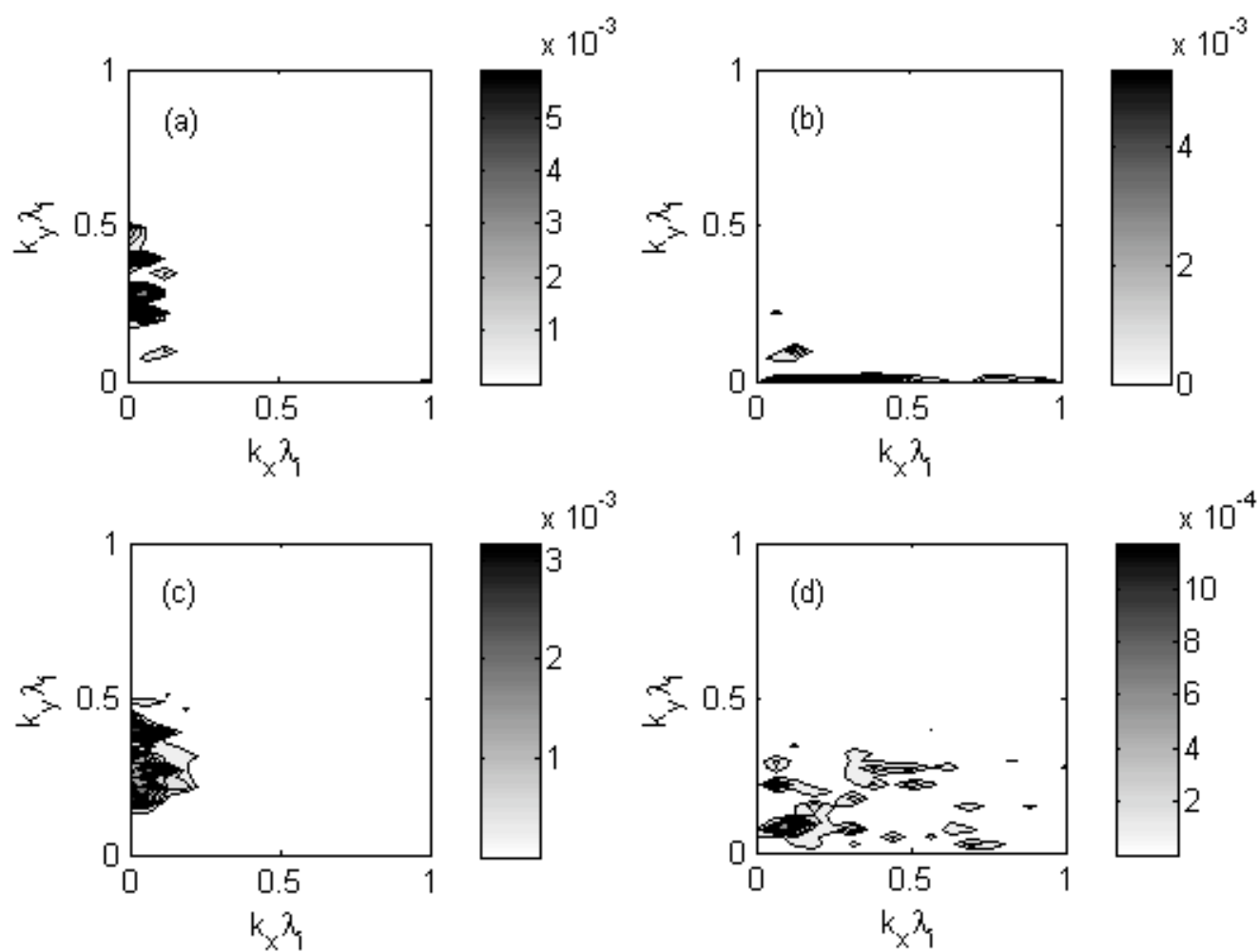


Figure 6

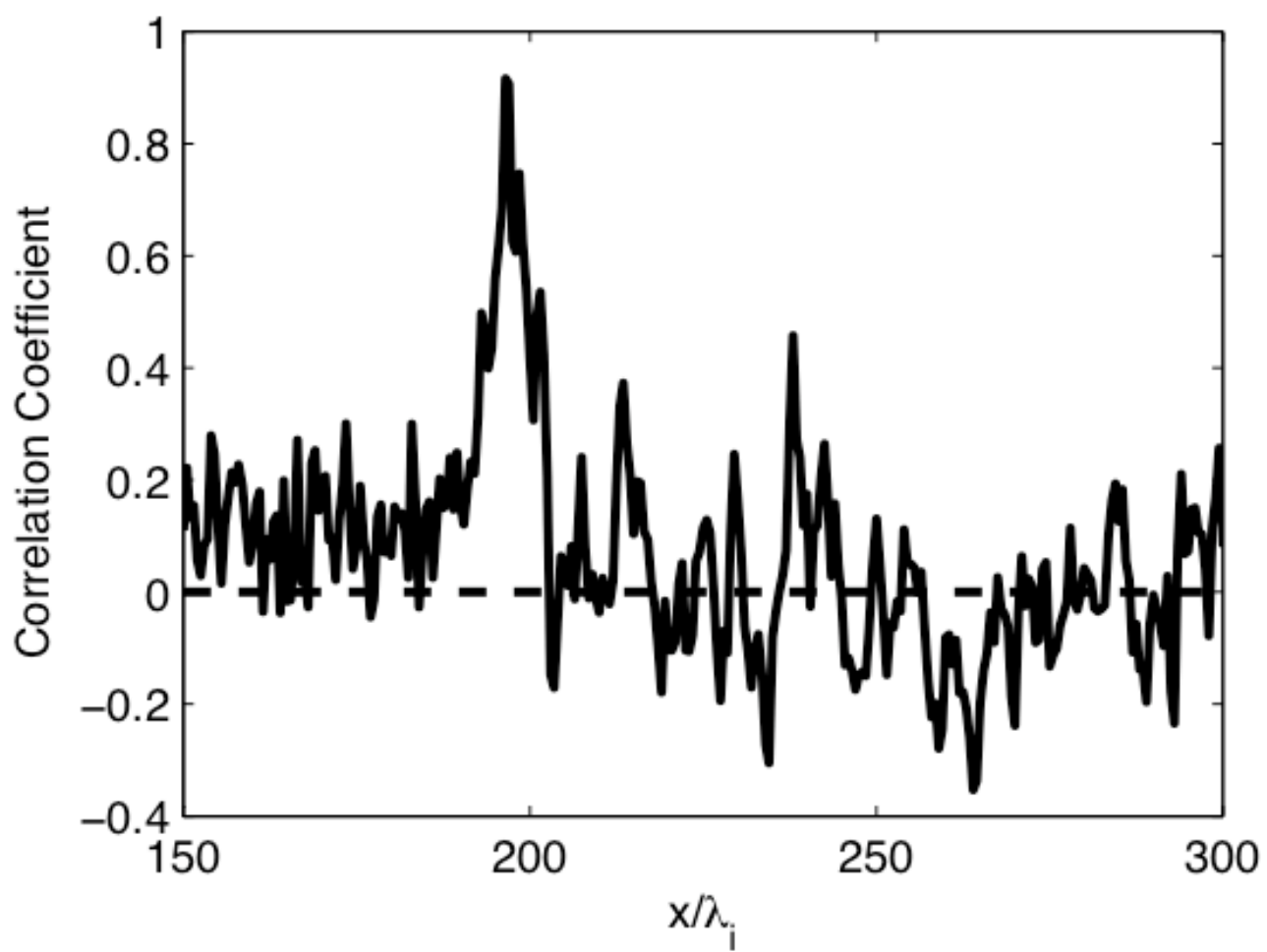


Figure 7

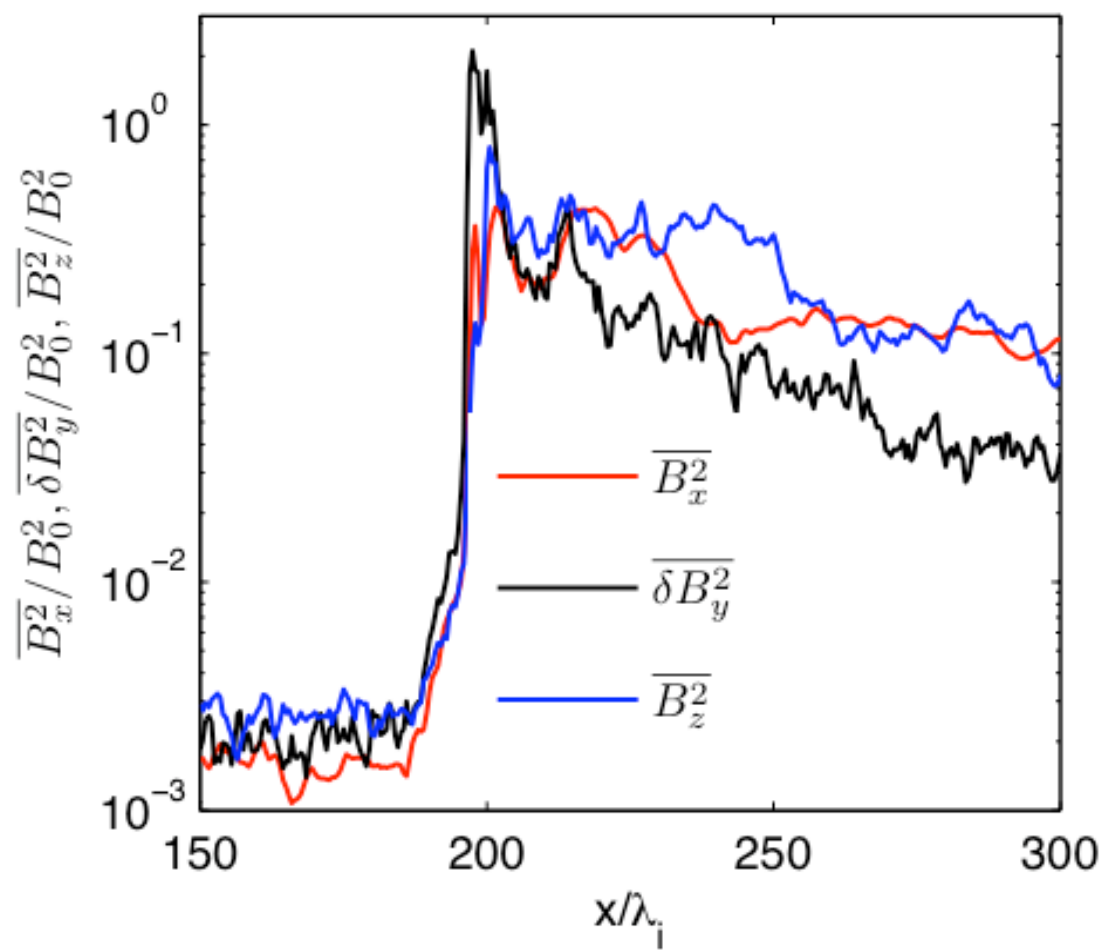


Figure 8

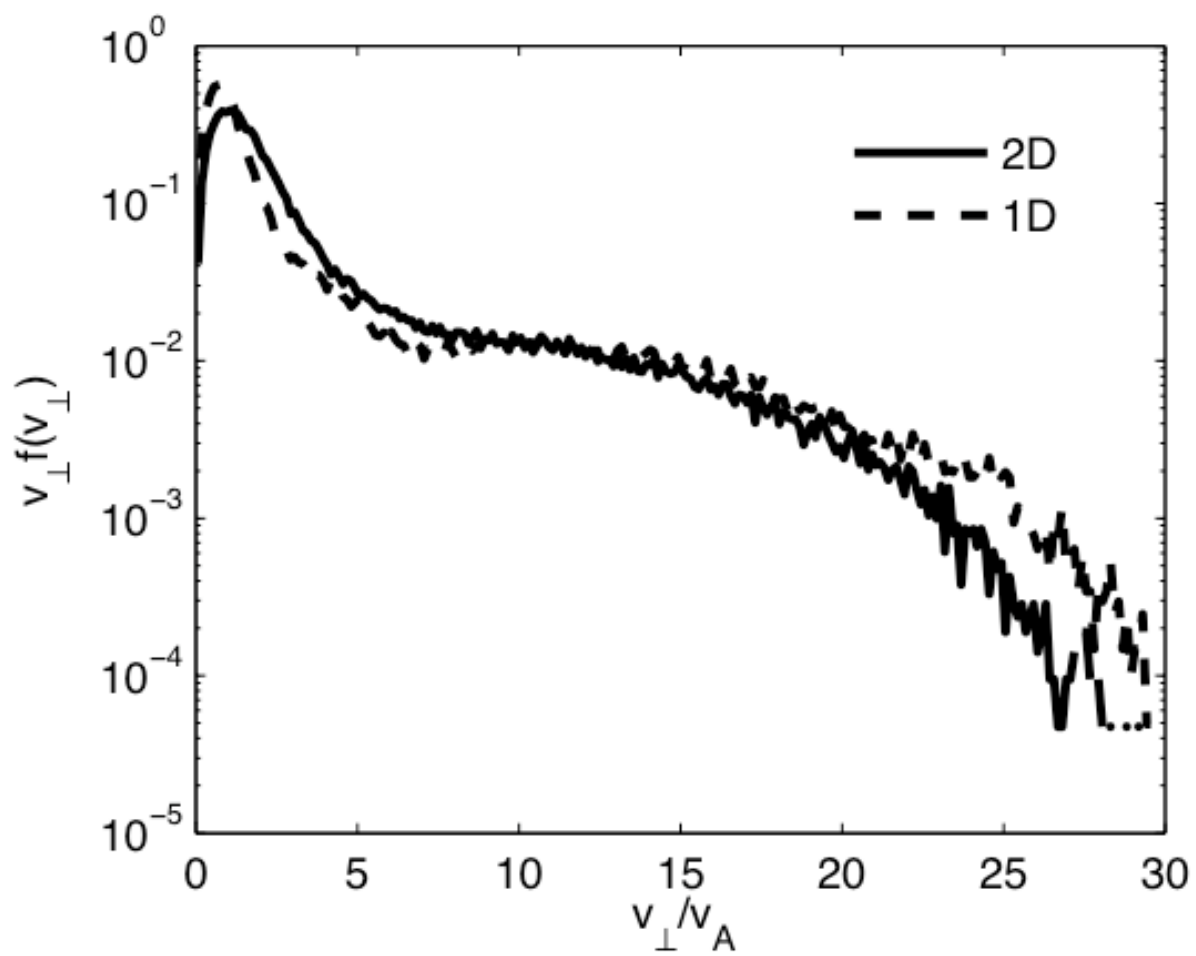


Figure 9

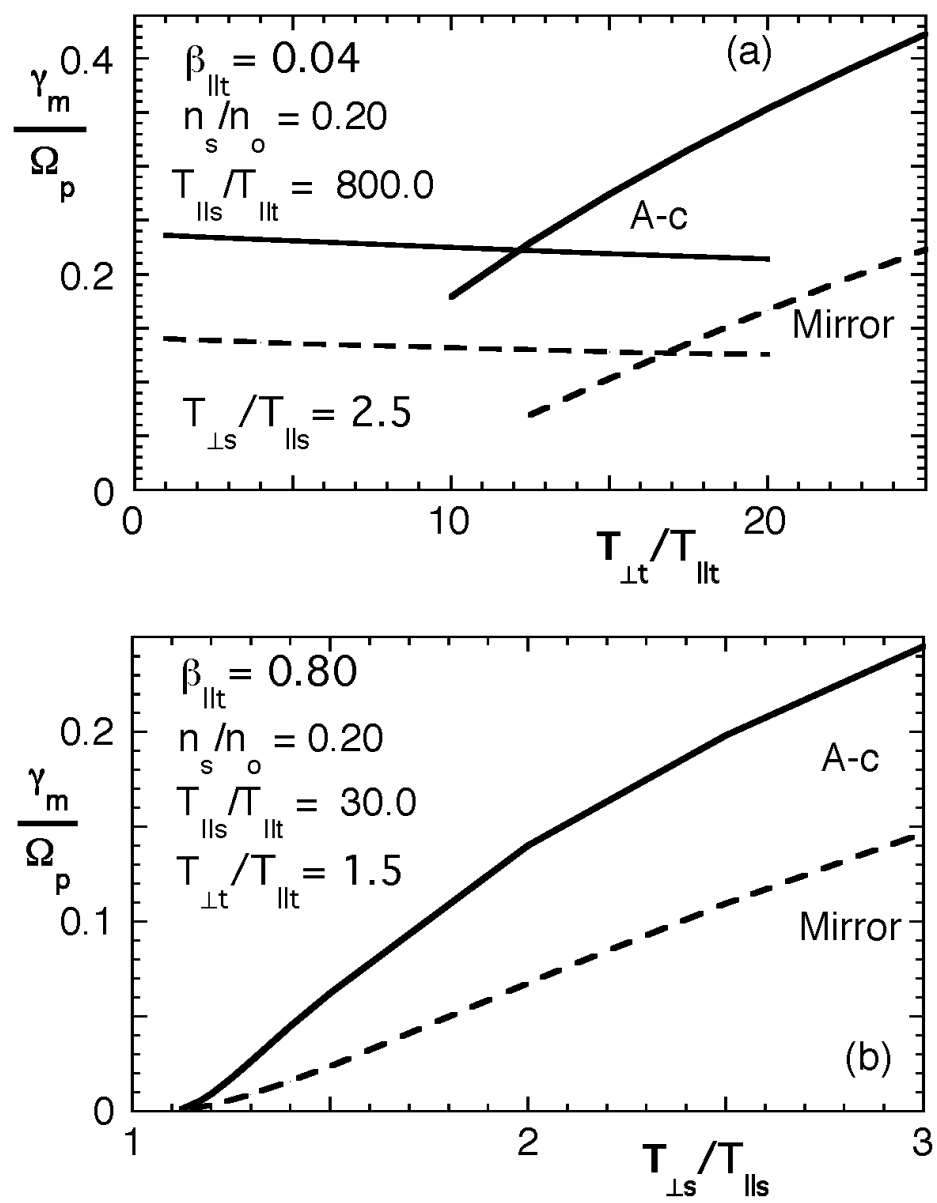


Figure 10

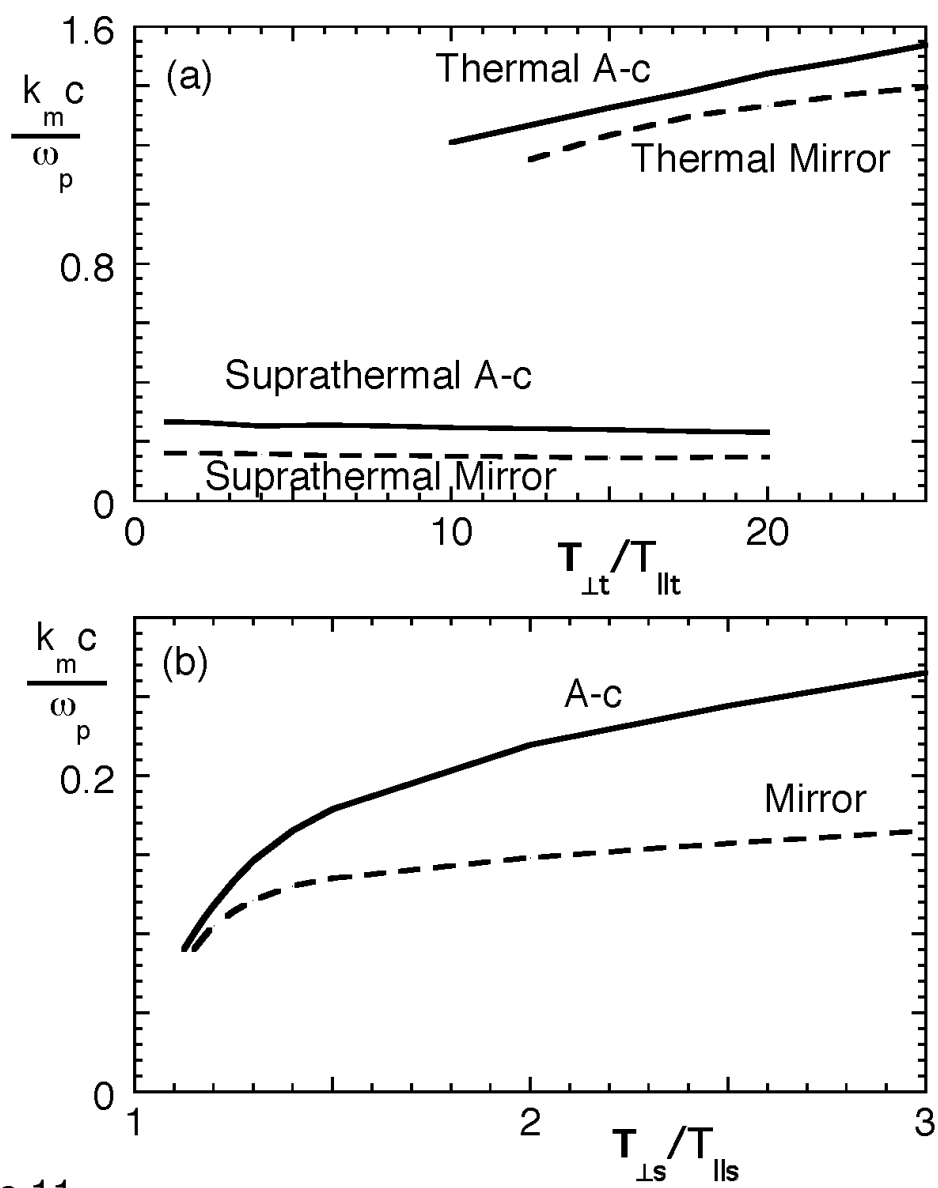


Figure 11

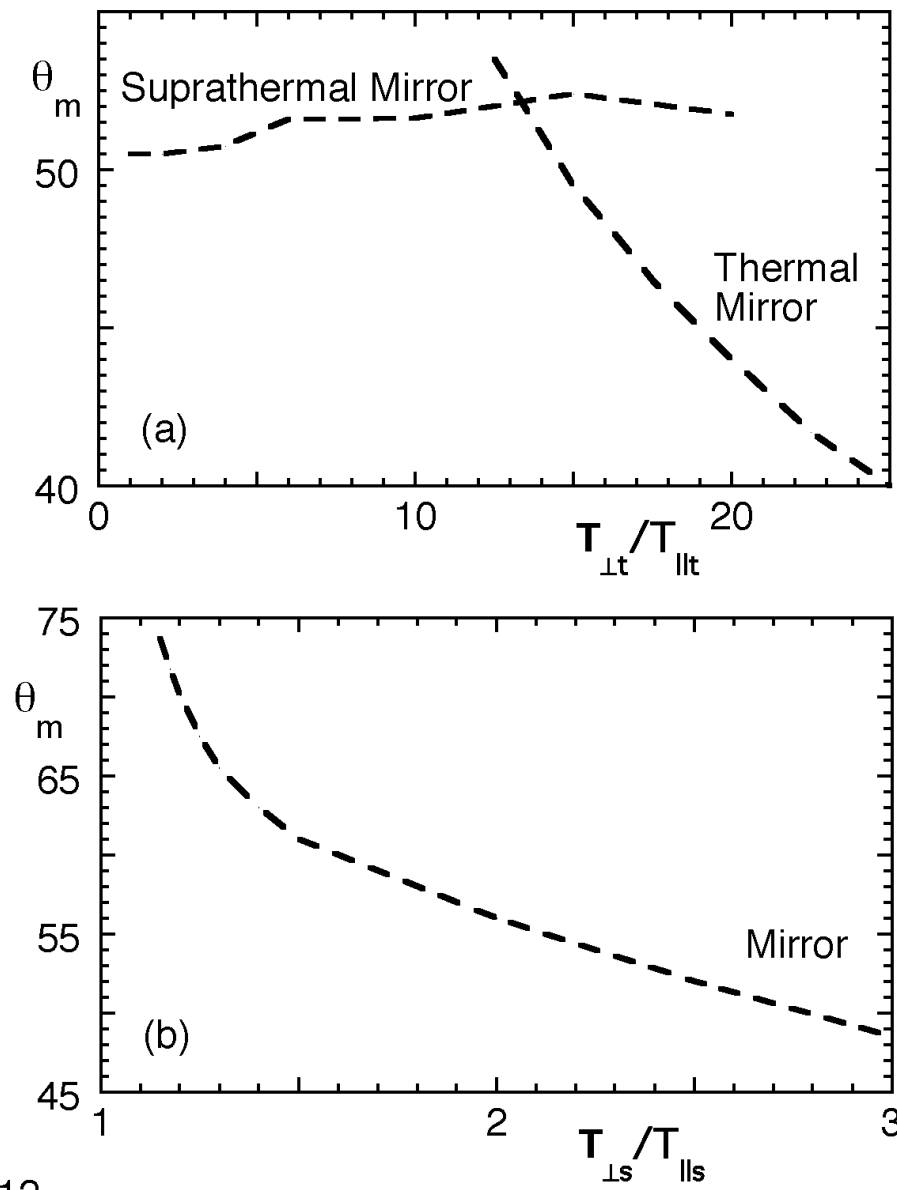


Figure 12